electronics

MDPI

Article

Valveless Piezoelectric Pump with Reverse Diversion Channel

Yongming Yao [1,2], Zhicong Zhou [1], Huiying Liu [1], Tianyu Li [1,*] and Xiaobin Gao [1]

[1] School of Mechanical and Aerospace Engineering, Jilin University, Changchun 130025, China; ymyao@jlu.edu.cn (Y.Y.); zhouzc20@mails.jlu.edu.cn (Z.Z.); huiying20@mails.jlu.edu.cn (H.L.); gaoxb19@mails.jlu.edu.cn (X.G.)

[2] State Key Laboratory of Superhard Materials, Jilin University, Changchun 130025, China

* Correspondence: litianyu@jlu.edu.cn; Tel.: +86-1384-401-0051

Abstract: In order to reduce backflow and improve output performance, a valveless piezoelectric pump with a reverse diversion channel was produced. The channel was designed based on the structure of the Tesla valve, which has no moving parts and can produce a high-pressure drop during reverse flow. Therefore, this special flowing channel can reduce the backflow of a valveless piezoelectric pump, which has the characteristic of one-way conduction. This work first revealed the relationship between the main structural parameters of the Tesla valve and the kinetic energy difference of liquid. Then, by using simulation software, the structure was verified to have the characteristics of effective suppression of the backflow of valveless piezoelectric pumps. Through setting multiple simulations, some important parameters that include the optimal height between the straight channels (H), the optimal angle (α) between the straight channel and the inclined channel, as well as the optimal radius (R) of the channel were confirmed. Finally, a series of prototypes were fabricated to test the output performance of this valveless piezoelectric pump. Comparing the experimental results, the optimal parameters of the Tesla valve were determined. The results suggest that when the parameters of the Tesla valve were H = 8 mm, α = 30°, and R = 3.4 mm, the output performance of this piezoelectric pump became best, which had a maximum flow rate of 79.26 mL/min with a piezoelectric actuator diameter of 35 mm, an applied voltage of 350 $V_{p\text{-}p}$, and a frequency of 28 Hz. The effect of this structure in reducing the return flow can be applied to fields such as agricultural irrigation.

Keywords: valveless piezoelectric pump; backflow; tesla valve; flow rate

Citation: Yao, Y.; Zhou, Z.; Liu, H.; Li, T.; Gao, X. Valveless Piezoelectric Pump with Reverse Diversion Channel. *Electronics* **2021**, *10*, 1712. https://doi.org/10.3390/electronics10141712

Academic Editor: Flavio Canavero

Received: 23 June 2021
Accepted: 15 July 2021
Published: 17 July 2021

1. Introduction

The piezoelectric pump, as a branch of micropump, because of its advantages of easy miniaturization, zero electromagnetic interference, and low noise, is greatly favored by scholars and widely used in many fields such as biomedicine [1–3], fuel cells [4–6], cooling systems [7–9], household appliances [10], as well as electronic sensors [11–13]. Among all kinds of piezoelectric pumps, valveless piezoelectric pumps possess the advantage of simple structure and high reliability, which receives much more attention.

Changing the physical structure of piezoelectric pumps to reduce its backflow and improve its output performance is a good method. Zhang et al. [14] analyzed several representative piezoelectric pumps from four perspectives: the structural design, working mode, optimization, and application of the piezoelectric pump. Huang et al. [15] analyzed and studied the output performance of valveless piezoelectric pumps with vortex diodes. Li et al. [16] conducted research on additive manufacturing technology related to piezoelectric pumps. Wang et al. [17] designed and researched a valveless piezoelectric pump based on a nozzle-shaped actuation chamber with an acoustic resonator profile. Dau et al. [18] designed a cross-junction channel for the valveless piezoelectric pump to increase the flow rate. Ma et al. [19] invented a piezoelectric pump based on centrifugal force through the principle of metal tube swing. Izzo et al. [20] designed a new type

of no-moving-part (NMP) valve for piezoelectric pumps. Zhang et al. [21] designed a spiral-tube-type valveless piezoelectric pump using the flow characteristics of the spiral tube. Zhang et al. [22] designed a novel bidirectional valveless piezoelectric micropump using the synthetic jet effect. However, there is a common backflow problem with valveless piezoelectric pumps, which is one of the biggest drawbacks. Therefore, several scholars have investigated piezoelectric pumps in terms of various structures [23,24] and applications [25–28]. In 2008, Tanaka et al. [29] used polymethyl methacrylate as a substrate and traditional machining technology to manufacture the prototype. Two kinds of pumps with nozzle depths of 0.5 and 0.2 mm were prepared, and the influence of nozzle depth on pump flow rate was studied. The maximum flow rate of the pump at 400 Pa was 17 mL/min when the resonant frequency was about 6 kHz and the sinusoidal voltage was 30 $V_{p\text{-}p}$. In 2014, Huang et al. [30] used fractal theory to analyze the flow resistance of Y-shaped branching tubes and the flow rate of the pump. A valveless piezoelectric pump with Y-shaped branching tubes with different fractal dimensions of diameter distribution was prepared. The experimental results showed that the flow rate of the pump increased with the fractal dimension of the pipe diameter. When the fractal dimension was 3, the maximum flow rate of the valveless pump was 29.16 mL/min under a 100 $V_{p\text{-}p}$ (13 Hz) power supply. In 2020, Zhao et al. [31] designed and manufactured a valveless piezoelectric pump with a multi-order meniscus resistive fluid structure in combination with 3D printing technology. When the order of the meniscus structure was quadruple and the input driving voltage and frequency were 220 $V_{p\text{-}p}$ and 82 Hz, respectively, the maximum output flow of the piezoelectric pump was 286 mL/min. These structures can reduce liquid backflow to a certain extent and provide a certain reference for the improvement of the structure.

Recently, studies have analyzed the application of Tesla valves in pumps. The Tesla valve is a passive one-way valve with a fixed geometry, which has one-way conduction characteristics and can replace a movable valve [32]. In 2020, Heng et al. [33] designed a centrifugal pump model based on the Tesla vane pump for conveying mud and multiphase flow, and they conducted preliminary experimental tests. Tran et al. [34] developed a valveless micropump based on the combined principle of the nozzle and Tesla element to correct the synthetic jet, which can work under low voltage. However, there is still little research on the Tesla valve in the direction of piezoelectric pumps, and there is a lack of specific research on the structural parameter design and performance of the Tesla valve.

In this study, in order to improve the output performance of valveless piezoelectric pumps, a valveless piezoelectric pump with a reverse diversion channel was presented. The structure was designed based on the principle of the Tesla valve, using its one-way conduction characteristics to inhibit the backflow of valveless piezoelectric pumps. Based on the structure mentioned in the next section, we mainly studied the influence of the height between the straight channels (H), the angle (α) between the straight channel and the inclined channel, as well as the radius of the channel (R) on the output performance of the piezoelectric pump, and we analyzed its theory. We then simulated it through simulation software and finally manufactured it through 3D printing technology to test the flow rate at different influencing factors. Comparing the experimental data, the best structural performance parameters could be obtained.

2. Design and Principle

2.1. Piezoelectric Pump Design

With reference to Figure 1, the configuration of the proposed piezoelectric pump with the Tesla valve is given. The size of the pump body is 100 mm × 50 mm × 20 mm. The internal and external pipe diameters are 4 and 6 mm, respectively, at the inlet and outlet. The piezoelectric pump is mainly composed of the pump cover, seal ring, pump body, piezoelectric actuator, seal shim, pump base with the Tesla valve, outlet pipe, and inlet pipe. A piezoelectric actuator is installed between the pump body and the pump cover, which is sealed by bolts, and the fluid is sealed in the pump body by a seal shim.

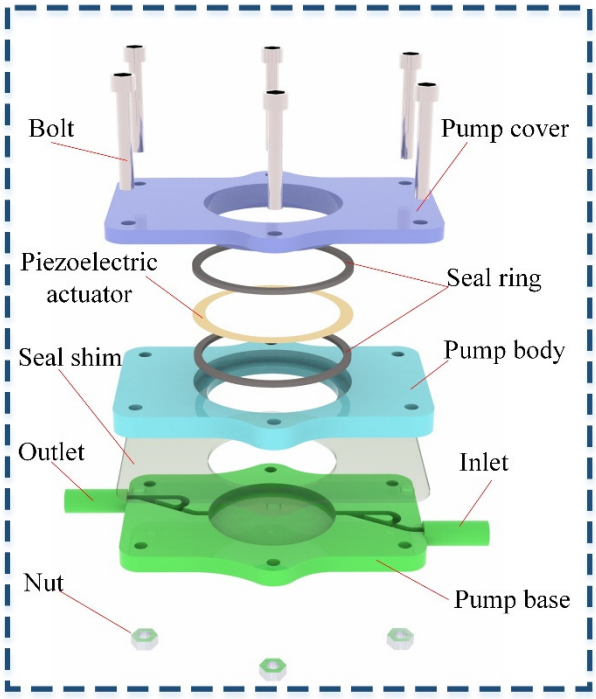

Figure 1. Structure of the valveless piezoelectric pump with Tesla valve assembly.

The structure of the reverse diversion channel based on the principle of one-way conduction of the Tesla valve was designed. When the fluid flows forward, the total energy loss is small; when the fluid flows in the reverse direction, the energy loss is great. It can be concluded that the structure of the Tesla valve can reduce liquid backflow and has the characteristic of one-way conduction.

2.2. Working Principle of the Piezoelectric Pump

The internal pressure of the pump chamber changes periodically, when the piezoelectric actuator is excited by a sinusoidal signal to generate vibration. Due to the special structure of the Tesla valve, it makes the amount of liquid inflow and liquid outflow different, and the piezoelectric pump expresses a one-way conduction characteristic. The working principle of the valveless piezoelectric pump with the Tesla valve structure can be divided into two main stages: the liquid inflow and the liquid outflow.

Liquid inflow stage: from time t_0 to t_1, the piezoelectric actuator turns upward (Figure 2a), the volume of the pump chamber increases, the pressure reduces, and fluid enters the pump chamber through the inlet and the outlet. Based on the structural principle of the Tesla valve, it makes more fluid enter the pump chamber through the inlet and less fluid enter the pump chamber through the outlet.

Liquid outflow stage: from time t_1 to t_2, the piezoelectric actuator turns downward (Figure 2b), the volume of the pump chamber reduces, and the pressure increases while pushing the fluid flows out through the inlet and the outlet simultaneously. Due to the Tesla valve structure, more fluid outflows through the outlet and less fluid outflows through the inlet.

The difference in flow rate between the two stages results in the continuous operation of the piezoelectric pump. In the photograph of the working principle, the blue lines represent the high flow rate and the white lines represent the low flow rate. Besides, the direction of the arrow represents the direction of water.

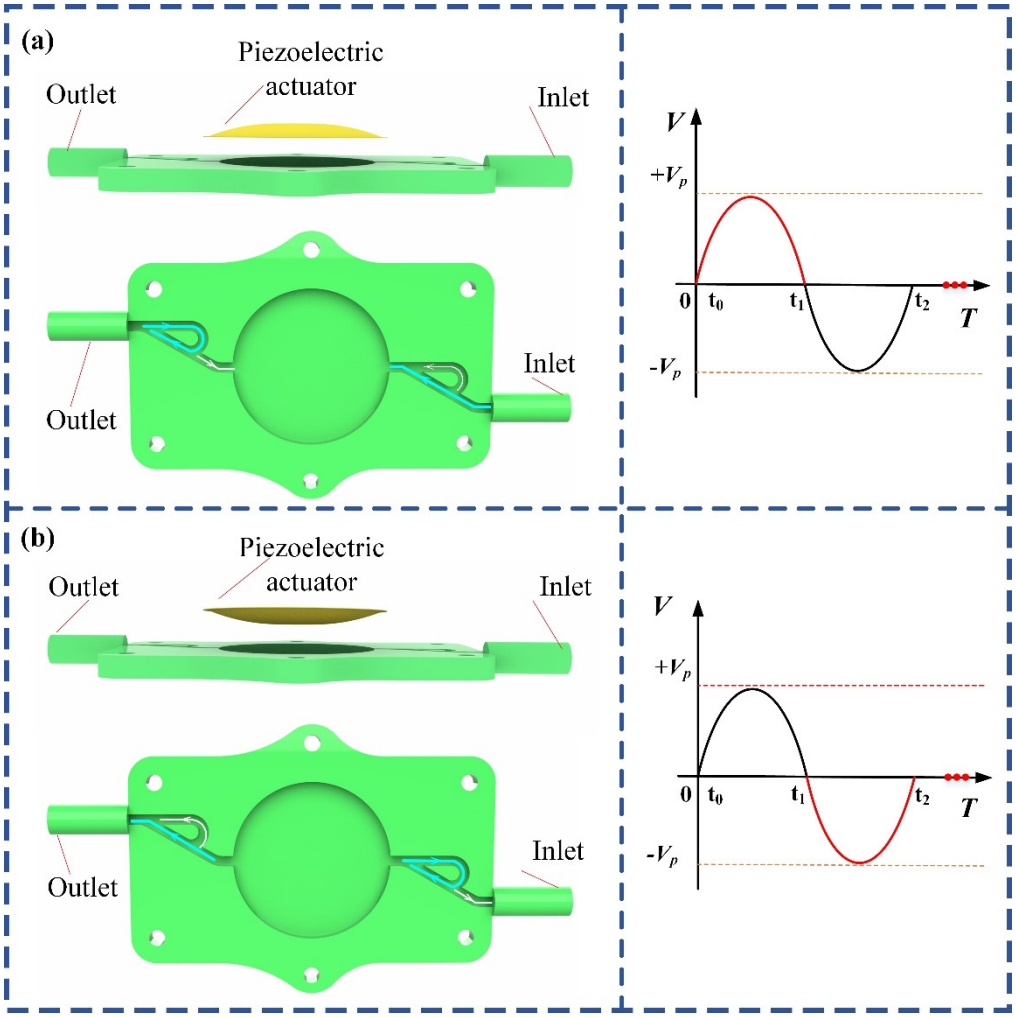

Figure 2. The valveless piezoelectric pump with the reverse diversion working principle: (**a**) liquid inflow; (**b**) liquid outflow.

3. Theoretical Analysis

As shown in Figure 3, H is the height between the straight channels, α is the angle between the straight channel and the inclined channel, and R is the optimal radius of the channel. In order to establish the relationship between the Tesla valve and the whole stage kinetic energy difference of the piezoelectric pump, the channel is divided into several parts. In the whole stage, including liquid inflowing and liquid outflowing, the main energy loss of the system includes two primary aspects: one is the friction loss, and the other is the local loss caused by the geometric shape and size change of the pipeline boundary. According to the Darcy–Weisbach Formula, the friction loss (h_f) and the location loss (h_j) are calculated as:

$$\begin{cases} h_f = \lambda \frac{l}{d} \frac{\overline{v}^2}{2g} \\ h_j = \xi \frac{\overline{v}^2}{2g} \end{cases} \quad (1)$$

where l is the pipe length through which water flows; d is the equivalent inner diameter of the pipe; $\overline{v}$ is the average flow velocity through the pipe section; g is the acceleration of gravity; λ is the coefficient of pressure loss along friction, which is obtained by the Nigolas' curve and Moody diagrams; ξ is the local loss coefficient, which can be obtained according to the local loss coefficient table, and its value mainly depends on the local change in water flow, the geometry shape, and the size of the boundary. In this design, considering that the radius and horizontal angle of the curve channel are identical, the value of ξ is invariable.

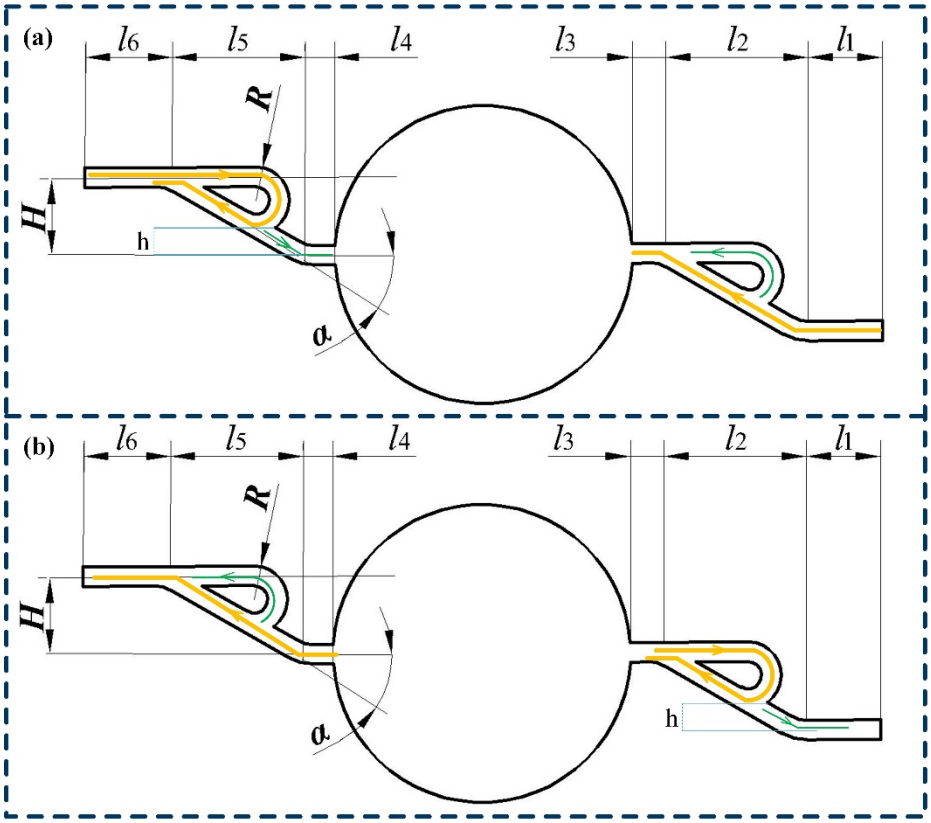

Figure 3. The structure of a Tesla valve: (**a**) liquid inflow; (**b**) liquid outflow.

At the stage of liquid inflow (as shown in Figure 3a), the friction loss of each part from l_1 to l_6 includes h_{f_1}, h_{f_2}, $\widehat{h}_{f_2}$,h_{f_3}, h_{f_4}, h_{f_5}, $\widehat{h}_{f_5}$, and h_{f_6}; the local loss of each part from l_1 to l_6 includes h_{j_1}, h_{j_2}, h_{j_3}, and h_{j_4}. According to the Darcy–Weisbach formula, the total friction loss and local loss at this stage are as follows:

$$\begin{cases} \sum\limits_{i=1}^{6} h_{f_i} = \lambda_1 \frac{l_1}{d} \frac{v^2}{2g} + \lambda_2 \frac{H}{d\sin\alpha} \frac{v_2^2}{2g} + \lambda_3 \frac{l_3}{d} \frac{v_3^2}{2g} + \lambda_4 \frac{l_4}{d} \frac{v_4^2}{2g} + \lambda_5 \frac{h}{d\sin\alpha} \frac{v_5^2}{2g} + \lambda_6 \frac{l_6}{d} \frac{\widehat{v}^2}{2g} \\ \sum \widehat{h}_f = \sum\limits_{\substack{u=2 \\ \delta=5}} \left(\widehat{h}_{f_u} + \widehat{h}_{f_\delta} \right) = \lambda_{\widehat{2}} \frac{R\pi + l_2 - R}{d} \frac{\widehat{v}_2^2}{2g} + \lambda_{\widehat{5}} \frac{R\pi + l_5 - R + \frac{H-h}{\sin\alpha}}{d} \frac{\widehat{v}_5^2}{2g} \\ \sum\limits_{\tau=1}^{4} h_{j_\tau} = \xi_1 \frac{v_1^2}{2g} + \xi_2 \frac{v_2^2}{2g} + \xi_3 \frac{v_5^2}{2g} + \xi_4 \frac{v_6^2}{2g} \end{cases} \quad (2)$$

In Equation (2), v and $\widehat{v}$ represent the inflow speed; v_1, v_2, $\widehat{v}_2$, v_3, v_4, v_5, $\widehat{v}_5$, and v_6, respectively, represent the average flow velocity of liquid in each part (from l_1 to l_6) at the stage of liquid inflow. In particular, both parts l_2 and l_5 include an inclined channel and a straight round channel. On the one hand, v_2 represents the average flow velocity of the inclined channel at part l_2; $\widehat{v}_2$ represents the average flow velocity of the straight round channel at part l_2; v_5 and $\widehat{v}_5$, respectively, represent the average flow velocity of the inclined channel and the average flow velocity of the straight round channel at part l_5. On the other hand, h_{f_2} and $\widehat{h}_{f_2}$, respectively, represent the friction loss in the inclined channel and the straight round channel at part l_2; h_{f_5} and $\hat{h}_{f_5}$, respectively, represent the friction loss and the straight round channel in the inclined channel at part l_5; d represents the inside diameter and is 2.8 mm.

At the stage of liquid outflow (as shown in Figure 3b), the friction loss of each part from l_1 to l_6 includes $\hat{h}_{f_1}$, $\hat{h}_{f_2}$, $\breve{h}_{f_2}$, $\hat{h}_{f_3}$, $\hat{h}_{f_4}$, $\hat{h}_{f_5}$, $\breve{h}_{f_5}$, and $\hat{h}_{f_6}$; the local loss of each part from l_1 to l_6 includes $\hat{h}_{j1}$, $\hat{h}_{j_2}$, $\hat{h}_{j_3}$, and $\hat{h}_{j_4}$. The total friction loss and local loss at this stage are as follows:

$$\begin{cases} \sum\limits_{i=1}^{6} \hat{h}_{f_i} = \lambda_{\hat{1}} \frac{l_1}{d} \frac{\hat{v}_1{}^2}{2g} + \lambda_{\hat{2}} \frac{h}{dsin\alpha} \frac{\hat{v}_2{}^2}{2g} + \lambda_{\hat{3}} \frac{l_3}{d} \frac{\hat{v}_3{}^2}{2g} + \lambda_{\hat{4}} \frac{l_4}{d} \frac{\hat{v}_4{}^2}{2g} + \lambda_{\hat{5}} \frac{H}{dsin\alpha} \frac{\hat{v}_5{}^2}{2g} + \lambda_{\hat{6}} \frac{l_6}{d} \frac{\hat{v}_6{}^2}{2g} \\ \sum \widetilde{h}_f = \sum\limits_{\substack{u=2 \\ \delta=5}} \left(\widetilde{h}_{f_u} + \widetilde{h}_{f_\delta} \right) = \lambda_{\widetilde{2}} \frac{R\pi + l_2 - R + \frac{H-h}{sin\alpha}}{d} \frac{\widetilde{v}_2{}^2}{2g} + \lambda_{\widetilde{5}} \frac{R\pi + l_5 - R}{dsin\alpha} \frac{\widetilde{v}_5{}^2}{2g} \\ \sum\limits_{\tau=1}^{4} \hat{h}_{j_\tau} = \xi_{\hat{2}} \frac{\hat{v}_2{}^2}{2g} + \xi_{\hat{4}} \frac{\hat{v}_4{}^2}{2g} + \xi_{\hat{5}} \frac{\hat{v}_5{}^2}{2g} + \xi_{\widetilde{2}} \frac{\widetilde{v}_2{}^2}{2g} \end{cases} \tag{3}$$

From Equation (3), $\hat{v}_1$, $\hat{v}_2$, $\widetilde{v}_2$, $\hat{v}_3$, $\hat{v}_4$, $\hat{v}_5$, $\widetilde{v}_5$, and $\hat{v}_6$, respectively, represent the average flow velocity of liquid in each part (from l_1 to l_6). $\hat{v}_2$ represents the average flow velocity of the inclined channel at part l_2; $\breve{v}_2$ represents the average flow velocity of the straight round channel at part l_2; $\hat{v}_5$ and $\widetilde{v}_5$, respectively, represent the average flow velocity of the inclined channel and the average flow velocity of the straight round channel at part l_5. $\hat{h}_{f_2}$ and $\widetilde{h}_{f_2}$, respectively, represent the friction loss in the inclined channel and the straight round channel at part l_2; $\hat{h}_{f_5}$ and $\widetilde{h}_{f_5}$, respectively, represent the friction loss in the inclined channel and in the straight round channel at part l_5.

In summary, the total energy loss ($\sum h_w$) can be obtained:

$$\sum h_w = \sum_{i=1}^{6} h_{f_i} + \sum \widehat{h}_f + \sum_{i=1}^{6} \hat{h}_{f_i} + \sum \widetilde{h}_f + \sum_{i=1}^{4} h_{\tau i} + \sum_{i=1}^{4} \hat{h}_{\tau_i} \tag{4}$$

According to the relationship between pressure, force, and energy, the following equation can be obtained:

$$\begin{cases} P_a = \rho g h \\ F = P_a S \\ W = Fl = \rho g h S = \rho g h l S \end{cases} \tag{5}$$

In this model, the head loss along the way is $h = l = h_f$, and the local head loss is $h = l = h_j$. The total energy loss can be obtained:

$$\sum W = \rho g \left(\sum_{i=1}^{6} h_{f_i} + \sum \widehat{h}_f + \sum_{i=1}^{6} \hat{h}_{f_i} + \sum \widetilde{h}_f + \sum_{i=1}^{4} h_{\tau i} + \sum_{i=1}^{4} \hat{h}_{\tau_i} \right)^2 S \tag{6}$$

where S is the cross-sectional area of the pipeline (2×2 mm^2).

According to the kinetic energy theorem, the following equation can be obtained:

$$E_Q - \sum W = \frac{1}{2} m v^2 + \frac{1}{2} m \widehat{v}^2 - \left(\frac{1}{2} m \hat{v}_1{}^2 + \frac{1}{2} m \hat{v}_6{}^2 \right) \tag{7}$$

where we define:

$$\begin{cases} E_{k1} = \frac{1}{2} m v^2 + \frac{1}{2} m \hat{v}^2 \\ E_{k2} = \frac{1}{2} m \hat{v}_1{}^2 + \frac{1}{2} m \hat{v}_6{}^2 \end{cases} \tag{8}$$

Among these equations, E_Q represents the total energy generated by the piezoelectric vibrator. E_{k1} is the initial kinetic energy and E_{k2} is the final kinetic energy.

From Equations (7) and (8), the following can be obtained:

$$E_Q - \sum W = E_{k1} - E_{k2} \tag{9}$$

From Equation (9), it can be concluded that under the condition that the energy generated by the piezoelectric vibrator (E_Q) is unchanged, the trends of kinetic energy difference ($E_{k1} - E_{k2}$) and the total loss energy ($\sum W$) are opposite. Therefore, the greater the energy that is lost, the smaller the kinetic energy differs, and the smaller the energy does work on the fluid, which will lead to a smaller flow rate. On the contrary, the lower the energy that is lost, the more the kinetic energy differs, and the more the energy does work on the fluid, resulting in a greater flow rate. At the same time, the kinetic energy difference is related to the energy loss and the important parameters of the Tesla valve (H, α, R).

4. Simulation Analysis

4.1. Simulation Settings

To determine the optimal parameters of the Tesla valve and verify the correctness of the working principle, ANSYS 15.0 was used for the finite element analysis (FEA) of the Tesla valve, and CFX software was used for the simulation of the flow field. Models were set-up with different heights (H = 5, 6, 7, 8, and 9 mm), different angles (α = 30, 45, 60, 75, and 90°), and different radii (R = 2.8, 3.1, 3.4, 3.7, and 4.0 mm). Although the Reynolds number of the structure was 20 and belongs to the range of laminar flow, due to the experimental research, the fluid can produce a violent impact when it flows through the pump chamber. Therefore, the k–ε turbulence equation was adopted. In the physical model, the fluid medium selected for the simulation was water, the fluid temperature was 25 °C, the density was 1000 kg/m^3, the inlet flow rate was set to 20 mm/s, and the outlet gauge pressure was set to 0 Pa. The roughness of the wall was set to 0.05 mm, which is consistent with the 3D printing layer. The parameters of the physical model are shown in Table 1. The best simulation parameter value can be determined by comparing the forward and reverse flow difference. The simulation data are shown in Figure 4. It can be seen that when H = 8 mm, α = 30°, and R = 4 mm, the flow velocity difference is largest. Compared with experimental research, when H = 8 mm and α = 30°, the flow velocity difference is largest. For the R factor, as 3.4 and 4.0 mm are both extreme points in the simulation process, it needs to be determined in conjunction with experimental results. Finally, it can be concluded through experimental analysis that 3.4 mm is the best parameter. Therefore, the Tesla valve with the optimal height (H = 8 mm), the optimal angle (α = 30°), and the optimal radius (R = 3.4 mm) was simulated.

Table 1. The parameters of the physical model.

Name	Parameters or Medium
Fluid medium	Water
Temperature	25 °C
Density	1000 kg/m^3
Inlet flow rate	20 mm/s
Outlet pressure	0 Pa
Roughness of wall	0.05 mm

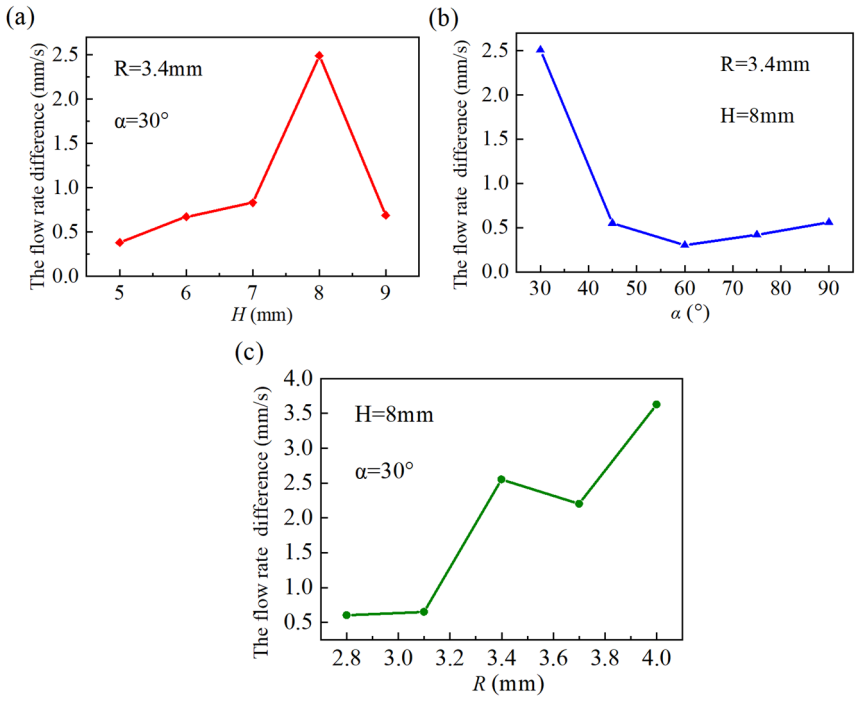

Figure 4. Forward and reverse flow velocity difference: (**a**) Flow velocity difference under different H. (**b**) Flow velocity difference under different α. (**c**) Flow velocity difference under different R.

4.2. Optimal Design Simulation

As is shown in Figure 5, the simulated velocity streamlines of the Tesla valve with the optimal height (H = 8 mm), the optimal angle (α = 30°), and the optimal radius (R = 3.4 mm) are presented. Figure 5a,b, respectively, represent the forward and reverse velocity streamlines. It can be seen that when the fluid flows forward into the chamber, most of the fluid directly flows along the inclined channel and a little of the fluid flows along the straight round channel at the inlet. Meanwhile, most of the fluid directly outflows the chamber along the inclined channel and a little of the fluid outflows along the straight round channel at the outlet, as shown in Figure 5a. When the fluid flows in the reverse direction into the chamber, most of the fluid flows along the inclined channel and the straight round channel at the inlet. At the same time, a little of the fluid outflows the chamber along the inclined channel and the straight round channel at the outlet, as shown in Figure 5b. By comparing the simulation outlet velocity of the forward and reverse flow, it is clear that the outlet velocity of the forward flow (22.8 mm/s) is greater than the outlet velocity of the reverse flow (20.4 mm/s). It can prove that the valveless piezoelectric pump with the reverse diversion channel can reduce the backflow and has the characteristic of one-way conduction.

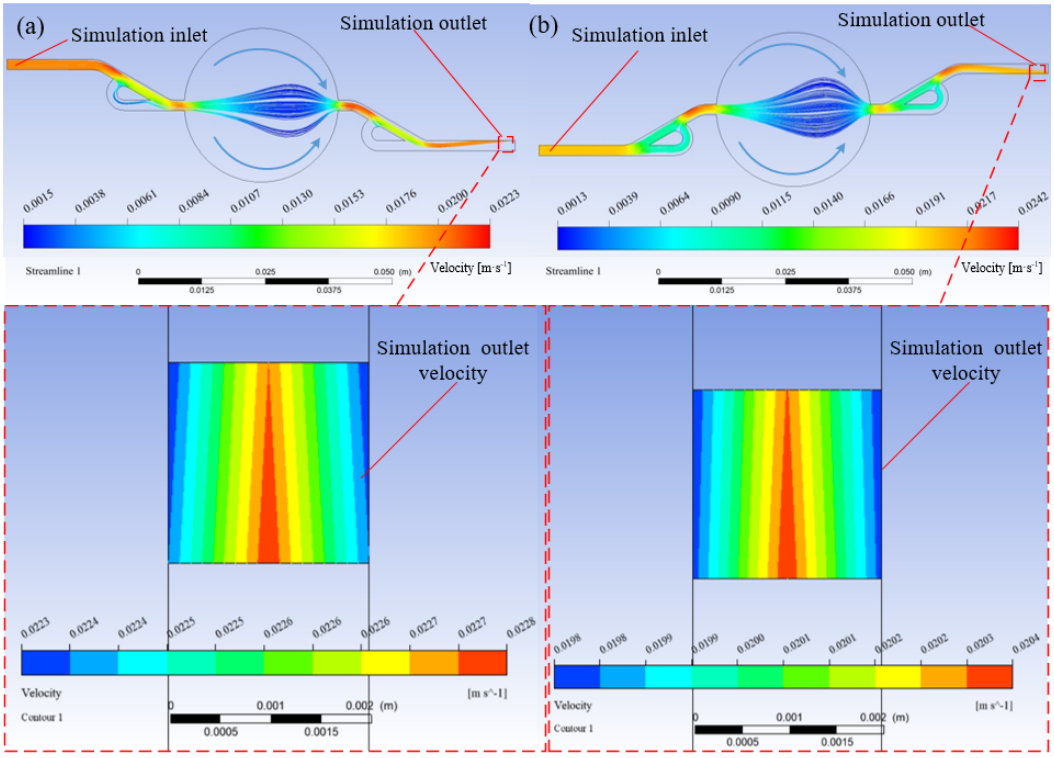

Figure 5. The forward and reverse flow simulation diagram of the optimal structure: (**a**) The forward velocity streamlines. (**b**) The reverse velocity streamlines.

5. Experimental Research

In order to further verify the effectiveness of the valveless piezoelectric pump with the reverse diversion channel design, experimental tests are essential. At first, several sets of piezoelectric pump prototypes were designed and manufactured; five sets of data with a channel height H of 5–9 mm (the interval is 1 mm), channel angle α of 30–90° (the interval is 15°), and channel radius R of 2.7–4.0 mm (the interval is 0.3 mm) were selected to make a piezoelectric pump prototype, as shown in Figure 6. The parameter values of the test prototype were consistent with those of the simulation model. Then, the output performance of the piezoelectric pump under different design parameters was tested. Finally, comparing the experimental results, the optimal parameters of the Tesla valve were determined. The characteristics of the piezoelectric actuator were as follows: the diameters of the copper substrate, ceramic plate, and piezoelectric film, and the total thicknesses were 35, 25, 0.1, and 0.5 mm.

The test system was established, as shown in Figure 7. The main test devices included a waveform generator (DG 4162, Beijing RIGOL Technology, Beijing, China), a power amplifier (HSA 4051, NF, Yokohama, Japan), an electronic balance, two beakers, and a bracket. Changing the voltage and frequency of the driving signal to react on the piezoelectric actuator can control the output level of the piezoelectric pump. The output flow rate of the piezoelectric pump was also measured.

The flow rate test was mainly divided into three parts. In the first part, the experimental steps were as follows: first, under a specific voltage, the output characteristics of the piezoelectric pump at different frequencies (from 1 Hz to no flow time) were tested; by comparing the flow rate, the optimal frequency can be obtained. Then, under the optimal frequency, the relationships between the voltage and output flow of piezoelectric micropumps with the height of the Tesla valve were tested mainly once per 10 V using a signal generator from 70 to 350 $V_{p\text{-}p}$. Similarly, by comparing the flow rate, the optimal voltage can be acquired. Finally, under the optimal voltage, the output characteristics of

the piezoelectric pump at different frequencies (from 17 to 42 Hz) were tested. In summary, under the optimal frequency, the relationships between voltage and output flow of the piezoelectric micropump can be obtained. Under the optimal voltage, the relationships between frequency and output flow of the piezoelectric micropump can also be obtained. In the second part, using the same experimental method, the connection between the angle of the channel α and the flow rate was established. In the third part, establishing the connection between the radius of the channel R and the flow rate, the test method was the same as the first part.

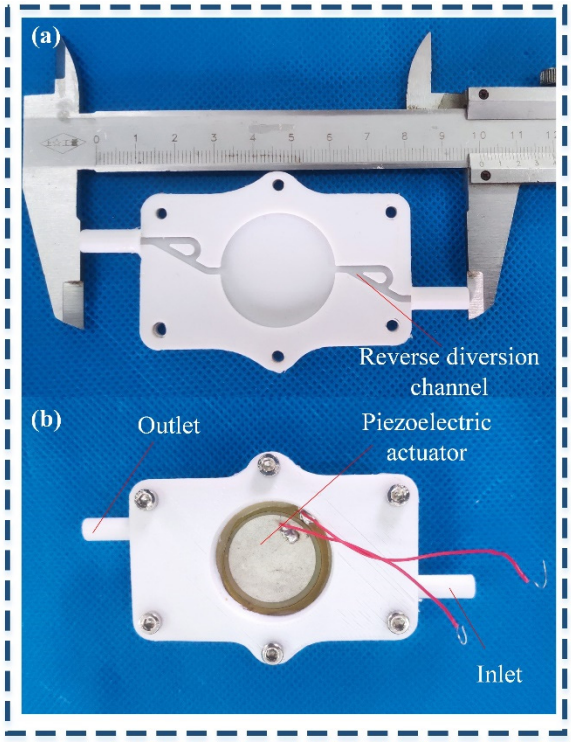

Figure 6. (**a**) Parts drawing of the valveless piezoelectric pump with reverse diversion channel (Tesla valve) with fluid guiding body; (**b**) prototype of the valveless piezoelectric pump with reverse diversion channel (Tesla valve).

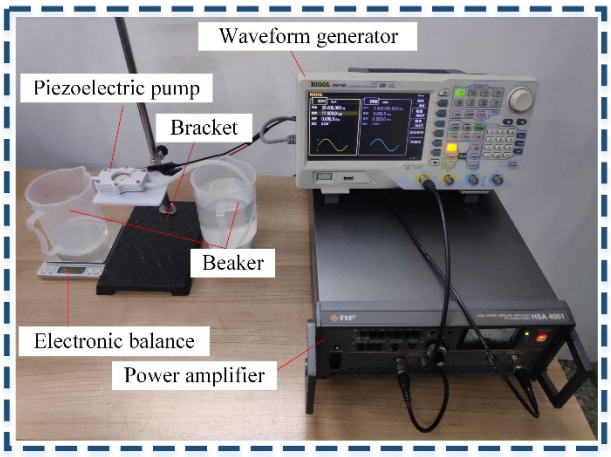

Figure 7. The photograph of the experimental system.

The output flow rate of the pump as a function of voltage and frequency with different design parameter values of the height of the straight channel H is as shown in Figure 8. It can be seen that with the increase in voltage, the flow rate linearly increases at the

optimum frequency, because with the climb in voltage, the deformation displacement in the piezoelectric actuator rises, which makes the change in pump chamber volume increase, and the flow rate augment. Under the optimum voltage, with the increase in frequency, the flow rate first increases and then decreases. The reason why the flow rate decreases is that when the driving frequency of the piezoelectric actuator is too high, the deformation of the piezoelectric actuator decreases, and when the vibration direction changes too fast, the volume change of the pump chamber can cause the pressure to change too fast and the pressure in the chamber to decrease. As can be seen from the frequency–flow curve, when H = 7 mm, f = 30 Hz, due to the experimental system reaching resonant frequency, and the flow rate suddenly increases to the maximum. Therefore, spikes will occur. Meanwhile, the various piezoelectric pumps perform best at frequencies between 24 and 32 Hz and have better low-frequency output characteristics. As shown in Figure 9, it is obvious that when the design parameters of height H increases, the best flow rate first increases and then decreases. As H increases, compared with the three-dimensional model shown in Figure S1 and Table S1 (Supporting Information), the length of the arc channel increases, and the effect of suppressing the return flow (the fluid flows from the outlet during the scheduling outflow) is enhanced. Although the loss along the way increases at this time, the flow rate will still increase. When the H value is large, the length of the inclined flow path continues to increase, and the loss along the way continues to increase. At this time, the effect of suppressing the return flow is worse than the energy loss caused by the loss along the way, so the flow rate will drop first. Therefore, changing the design parameters of height H will affect the output performance of the piezoelectric pump. When H = 8 mm, f = 28 Hz, and V = 350 $V_{p\text{-}p}$, the output performance of the piezoelectric pump is best.

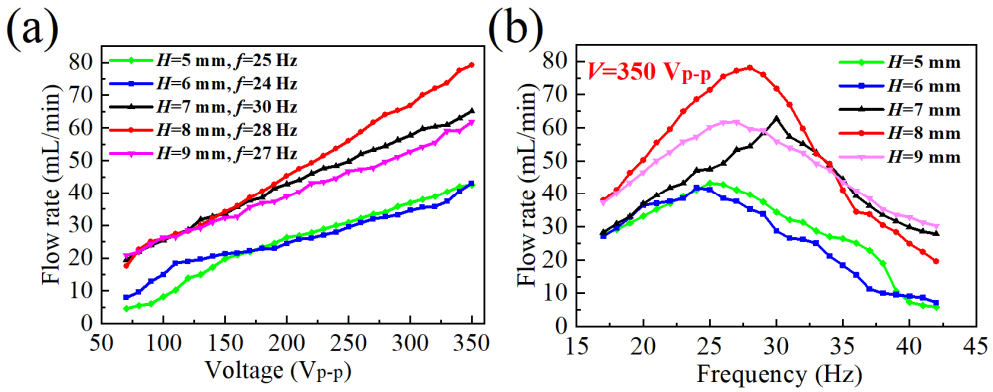

Figure 8. The trend of flow rate with the height of the Tesla valve at different voltages and frequencies: (**a**) the voltage–flow curve; (**b**) the frequency–flow curve.

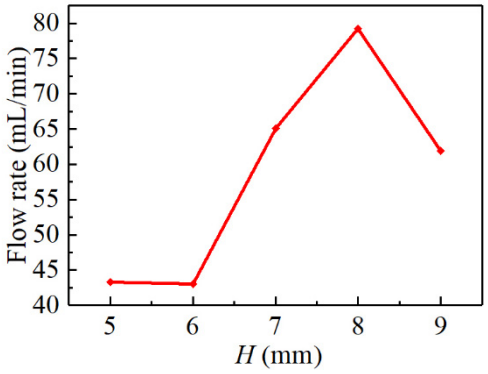

Figure 9. Corresponding maximum flow under different H.

When H = 8 mm, the relationships between voltage, frequency, and output flow of piezoelectric micro-pumps with different design parameter values of the angle of the

channel α are as shown in Figure 10. It highlights the continuous growth of the flow rate with the increase in the voltage at the optimum frequency of each prototype. In particular, from the frequency–flow curve, when α = 75° and the frequency increases from 38 to 42 Hz, the trend of flow rate decline drops from 19.64 to 0 mL/min. For the reason that air bubbles generated during the flow of the liquid, the output performance of the piezoelectric pump was affected. As is shown in Figure 11, with the increase in the angle α, the flow rate first decreases and then increases. The reason seems to be that as the angle increases, the loss along the way increases, so the flow rate will decrease. When the angle continues to increase, comparing with the three-dimensional model shown in Figure S2 and Table S2 (Supporting Information), the arc length of the arc flow channel at this time increases, which enhances the effect of suppressing the backflow, so the flow rate will increase. When H = 8 mm, α = 30°, f = 28 Hz, and V = 350 $V_{p\text{-}p}$, the piezoelectric pump can reach the best flow rate.

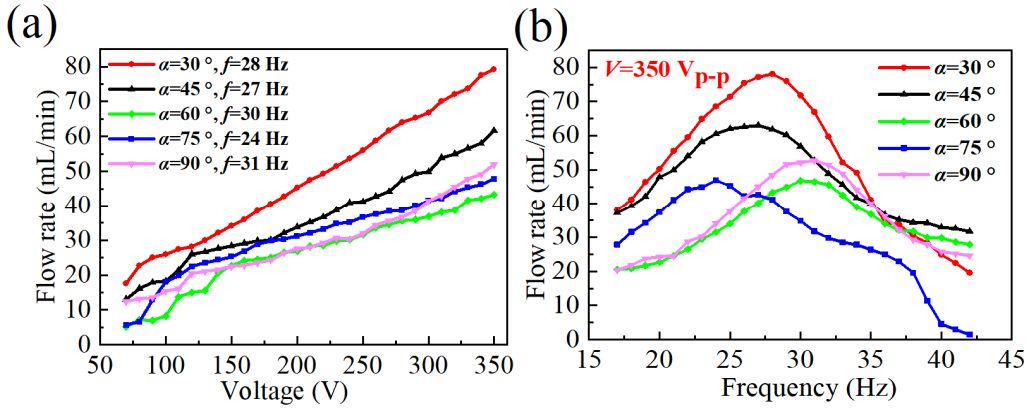

Figure 10. The trend of flow rate with the angle of the Tesla valve at different voltages and frequencies: (**a**) the voltage–flow curve; (**b**) the frequency–flow curve.

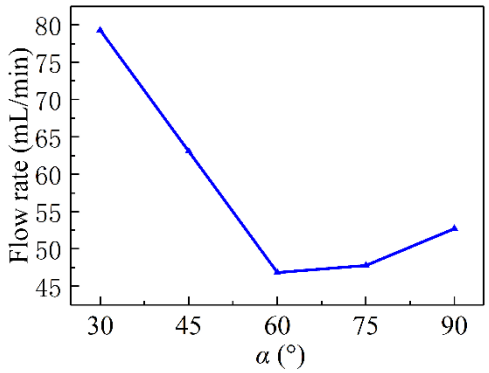

Figure 11. Corresponding maximum flow under different α.

After gaining the two parameters of H = 8 mm and α = 30°, the determination of the third parameter (the radius of the channel R) was tested. The testing results were as follows: from Figure 12, it can be shown that the trend of flow rate with the radius of the Tesla valve at different voltages and frequencies is the same as testing H and α. From Figure 13, as the radius increases, the flow rate first increases and then decreases. The possible reason is that when the radius increases, in the scheduling stage (when the piezoelectric sheet moves downward), the effect of inhibiting the discharge of fluid from the outlet becomes greater. When the radius increases to a large enough size, the loss along the way during the return flow will increase, and the returned liquid will not have enough power to return to the chamber along the long oblique flow path. Therefore, the maximum flow rate will decrease. Besides, when R = 3.4 mm, the system has reached the resonance state. With R = 4 mm, there are more bubbles in the experiment under the resonance state, which

affects the output flow of the channel. However, in the simulation stage of R = 4 mm, due to the influence of bubbles being ignored, the effect of the flow rate caused by the increase in the radius is greater than the effect of the loss along the way, so the flow rate is largest in the simulation stage of R = 4 mm. Therefore, there will be differences between simulation and experimental results when R = 4 mm. Considering the specific conditions of the experiment, R = 3.4 mm is selected as the best parameter. When H = 8 mm, $\alpha = 30°$, R = 3.4 mm, f = 28 Hz, and V = 350 $V_{p\text{-}p}$, the piezoelectric pump has the best flow rate, which is 79.26 mL/min.

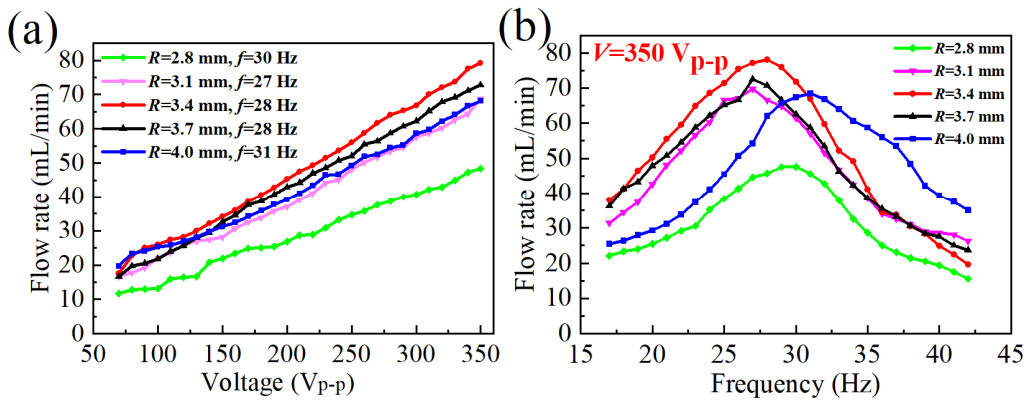

Figure 12. The trend of flow rate with the radius of the Tesla valve at different voltages and frequencies: (**a**) the voltage–flow curve; (**b**) the frequency–flow curve.

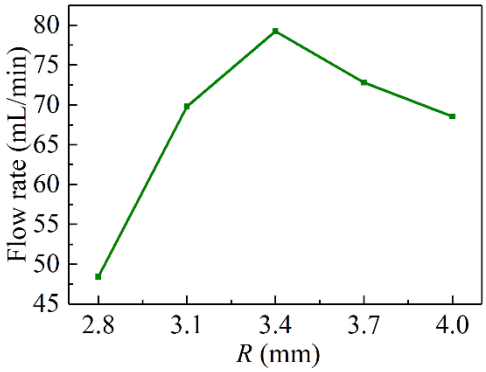

Figure 13. Corresponding maximum flow under different R.

Finally, after conducting an experimental comparison of three sets of parameters, the optimal parameters of the Tesla valve were determined. The results suggest that when the parameters of the Tesla valve are H = 8 mm, $\alpha = 30°$, and R = 3.4 mm, the output performance of this piezoelectric pump becomes best, which has a maximum flow rate of 79.26 mL/min with a piezoelectric actuator diameter of 35 mm, an applied voltage of 350 $V_{p\text{-}p}$, and a frequency of 28 Hz.

6. Conclusions

This paper aimed to obtain the best output performance of a valveless piezoelectric pump with an optimal channel structure size. First, based on the Tesla valve principle, a valveless piezoelectric pump with a reverse diversion channel was proposed. Secondly, through theoretical and simulation analysis, it was verified that the structure has the characteristics of reducing backflow and one-way conduction. Finally, a series of prototypes were made to test the output performance of this valveless piezoelectric pump, and the best structural parameters were obtained by comparing the experimental data. This piezoelectric pump with the Tesla valve of H = 8 mm, $\alpha = 30°$, and R = 3.4 mm had the best performance, and it was fabricated through 3D printing technology. The maximum

flow rate was 79.26 mL/min, when driven by the applied voltage of 350 V_{p-p} at 28 Hz. The effect of this structure in reducing the return flow can be applied to fields such as agricultural irrigation.

Supplementary Materials: The following are available online at https://www.mdpi.com/article/10.3390/electronics10141712/s1, Figure S1: the length of the arc channel in different H. Table S1: the length of the arc channel in different H. Figure S2: the length of the arc channel in different α. Table S2: the length of the arc channel in different α.

Author Contributions: Software, data curation, writing—original draft preparation, Y.Y. and Z.Z.; methodology, validation, Y.Y. and H.L.; writing—review and editing, T.L.; supervision, project administration, T.L. and X.G.; funding acquisition, Y.Y. All authors have read and agreed to the published version of the manuscript.

Funding: This work is supported by the Science and Technology Development Project of Jilin Province (Grant No. 20190303061SF) and the National Natural Science Foundation of China (Grant No. 51805200).

Acknowledgments: This work is supported by the Science and Technology Development Project of Jilin Province.

Conflicts of Interest: The authors declare no conflict of interest.

References

1. Ma, H.K.; Chen, R.H.; Yu, N.S.; Hsu, Y.H. A miniature circular pump with a piezoelectric bimorph and a disposable chamber for biomedical applications. *Sens. Actuators A-Phys.* **2016**, *251*, 108–118. [CrossRef]
2. Liu, G.; Shen, C.; Yang, Z.; Cai, X.; Zhang, H. A disposable piezoelectric micropump with high performance for closed-loop insulin therapy system. *Sens. Actuators A-Phys.* **2010**, *163*, 291–296. [CrossRef]
3. Jenke, C.; Rubio, J.P.; Kibler, S.; Haefner, J.; Richter, M.; Kutter, C. The Combination of Micro Diaphragm Pumps and Flow Sensors for Single Stroke Based Liquid Flow Control. *Sensors* **2017**, *17*, 755. [CrossRef]
4. Yang, X.; Zhou, Z.; Cho, H.; Luo, X. Study on a PZT-actuated diaphragm pump for air supply for micro fuel cells. *Sens. Actuators A-Phys.* **2006**, *130*, 531–536. [CrossRef]
5. Park, J.H.; Seo, M.Y.; Ham, Y.B.; Yun, S.N.; Kim, D.I. A study on high-output piezoelectric micropumps for application in DMFC. *J. Electroceram.* **2013**, *30*, 102–107. [CrossRef]
6. Ma, H.K.; Huang, S.H.; Kuo, Y.Z. A novel ribbed cathode polar plate design in piezoelectric proton exchange membrane fuel cells. *J. Power Sources* **2008**, *185*, 1154–1161. [CrossRef]
7. Ma, H.-K.; Hou, B.-R.; Lin, C.-Y.; Gao, J.-J. The improved performance of one-side actuating diaphragm micropump for a liquid cooling system. *Int. Commun. Heat Mass Transf.* **2008**, *35*, 957–966. [CrossRef]
8. Ma, H.-K.; Chen, B.-R.; Gao, J.J.; Lin, C.-Y. Development of an OAPCP-micropump liquid cooling system in a laptop. *Int. Commun. Heat Mass Transf.* **2009**, *36*, 225–232. [CrossRef]
9. Bayomy, A.M.; Saghir, M.Z.; Yousefi, T. Electronic cooling using water flow in aluminum metal foam heat sink: Experimental and numerical approach. *Int. J. Therm. Sci.* **2016**, *109*, 182–200. [CrossRef]
10. Wang, C.-P.; Wang, G.-B.; Ting, Y. Analysis of dynamic characteristics and cooling performance of ultrasonic micro-blower. *Microelectron. Eng.* **2018**, *195*, 1–6. [CrossRef]
11. Zhang, Z.; Kan, J.; Cheng, G.; Wang, H.; Jiang, Y. A piezoelectric micropump with an integrated sensor based on space-division multiplexing. *Sens. Actuators A-Phys.* **2013**, *203*, 29–36. [CrossRef]
12. Lee, S.C.; Hur, S.; Kang, D.; Kim, B.H.; Lee, S.J. The performance of bioinspired valveless piezoelectric micropump with respect to viscosity change. *Bioinspir. Biomim.* **2016**, *11*. [CrossRef]
13. Zhang, Z.; Kan, J.W.; Wang, S.; Wang, H.; Ma, J.; Jiang, Y. Development of a self-sensing piezoelectric pump with a bimorph transducer. *J. Intell. Mater. Syst. Struct.* **2016**, *27*, 581–591. [CrossRef]
14. Li, H.; Liu, J.; Li, K.; Liu, Y. A review of recent studies on piezoelectric pumps and their applications. *Mech. Syst. Signal Process.* **2021**, *151*, 107393. [CrossRef]
15. Huang, J.; Zou, L.; Tian, P.; Wang, Y.; Zhang, Q. Development of a valveless piezoelectric pump with vortex diodes. *J. Micromech. Microeng.* **2019**, *29*. [CrossRef]
16. Li, H.; Liu, J.; Li, K.; Liu, Y. Piezoelectric micro-jet devices: A review. *Sens. Actuators A-Phys.* **2019**, *297*, 111552. [CrossRef]
17. Wang, S.S.; Huang, X.Y.; Yang, C. Valveless micropump with acoustically featured pumping chamber. *Microfluid. Nanofluid.* **2010**, *8*, 549–555. [CrossRef]
18. Dau, V.T.; Dinh, T.X.; Katsuhiko, T.; Susumu, S. A cross-junction channel valveless-micropump with PZT actuation. *Microsyst. Technol. Micro-Nanosyst. Inf. Storage Process. Syst.* **2009**, *15*, 1039–1044. [CrossRef]

19. Ma, Y.T.; Kong, F.R.; Pan, C.L.; Zhang, Q.; Feng, Z.H. Miniature tubular centrifugal piezoelectric pump utilizing wobbling motion. *Sens. Actuators A-Phys.* **2010**, *157*, 322–327. [CrossRef]
20. Izzo, I.; Accoto, D.; Menciassi, A.; Schmitt, L.; Dario, P. Modeling and experimental validation of a piezoelectric micropump with novel no-moving-part valves. *Sens. Actuators A-Phys.* **2007**, *133*, 128–140. [CrossRef]
21. Zhang, J.; Leng, X.; Zhao, C. A spiral-tube-type valveless piezoelectric pump with gyroscopic effect. *Chin. Sci. Bull.* **2014**, *59*, 1885–1889. [CrossRef]
22. Zhang, X.T.; Yang, S.; He, X.H.; Yuan, S.Q. *A Bidirectional Valveless Piezoelectric Micropump with Double Chambers Applying Synthetic Jet*; American Society Mechanical Engineers: New York, NY, USA, 2015.
23. Ma, H.-K.; Luo, W.-F.; Lin, J.-Y. Development of a piezoelectric micropump with novel separable design for medical applications. *Sens. Actuators A-Phys.* **2015**, *236*, 57–66. [CrossRef]
24. Wang, X.Y.; Ma, Y.T.; Yan, G.Y.; Huang, D.; Feng, Z.H. High flow-rate piezoelectric micropump with two fixed ends polydimethylsiloxane valves and compressible spaces. *Sens. Actuators A-Phys.* **2014**, *218*, 94–104. [CrossRef]
25. Iijima, Y.; Takemura, K.; Edamura, K. Droplet generating device for droplet-based mu TAS using electro-conjugate fluid. *Smart Mater. Struct.* **2017**, *26*. [CrossRef]
26. Valdovinos, J.; Carman, G.P. Development of a low-voltage piezohydraulic pump for compact hydraulic systems. *Smart Mater. Struct.* **2015**, *24*. [CrossRef]
27. Wei, Y.; Torah, R.; Yang, K.; Beeby, S.; Tudor, J. A novel fabrication process to realize a valveless micropump on a flexible substrate. *Smart Mater. Struct.* **2014**, *23*. [CrossRef]
28. Ren, Y.J.; Ma, Y.T.; Huang, D.; Chen, J.; Feng, Z.H. Elastic string check valves can efficiently heighten the piezoelectric pump's working frequency. *Sens. Actuators A-Phys.* **2016**, *244*, 126–132. [CrossRef]
29. Tanaka, K.; Dau, V.T.; Sakamoto, R.; Dinh, T.X.; Dao, D.V.; Sugiyama, S. Fabrication and Basic Characterization of a Piezoelectric Valveless Micro Jet Pump. *Jpn. J. Appl. Phys.* **2008**, *47*, 8615–8618. [CrossRef]
30. Huang, J.; Zhang, J.; Wang, S.; Liu, W. Analysis of the Flow Rate Characteristics of Valveless Piezoelectric Pump with Fractal-like Y-shape Branching Tubes. *Chin. J. Mech. Eng.* **2014**, *27*, 628–634. [CrossRef]
31. Zhao, D.; He, L.-P.; Li, W.; Huang, Y.; Cheng, G.-M. Experimental analysis of a valve-less piezoelectric micropump with crescent-shaped structure. *J. Micromech. Microeng.* **2019**, *29*. [CrossRef]
32. Nabavi, M. Steady and unsteady flow analysis in microdiffusers and micropumps: A critical review. *Microfluid. Nanofluid.* **2009**, *7*, 599–619. [CrossRef]
33. Heng, Y.G.; Han, Y.M.; Zhang, H.Y.; Zhang, W.B.; Bois, G.; Jiang, Q.F.; Wang, Z.W.; Liu, X.B. Tesla Bladed Pump (Disc Bladed Pump) Preliminary Experimental Performance Analysis. *Energies* **2020**, *13*, 4873. [CrossRef]
34. Tran, C.D.; Pham, P.H.; Nguyen, T.K.; Phan, H.P.; Dinh, T.; Nguyen, T.V.; Bui, T.T.; Chu, D.T.; Nguyen, N.T.; Dao, D.V.; et al. A new structure of Tesla coupled nozzle in synthetic jet micro-pump. *Sens. Actuators A-Phys.* **2020**, *315*. [CrossRef]